

AD _____

GRANT NO: DAMD17-94-J-4362

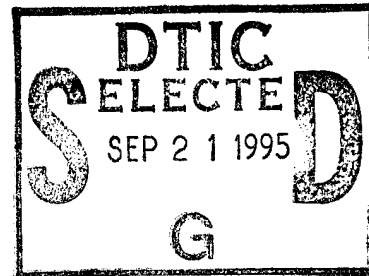
TITLE: "Development of Methods for Improved Breast Imaging Using Ultrasound"

PRINCIPAL INVESTIGATOR: Dr. John M. Reid
Dr. Athina P. Petropulu

CONTRACTING ORGANIZATION: Drexel University
Philadelphia, Pennsylvania 19104

REPORT DATE: July 26, 1995

TYPE OF REPORT: Annual



PREPARED FOR: U.S. Army Medical Research and Materiel Command
Fort Detrick, Maryland 21702-5012

DISTRIBUTION STATEMENT: Approved for public release;
distribution unlimited

The views, opinions and/or findings contained in this report are those of the author(s) and should not be construed as an official Department of the Army position, policy or decision unless so designated by other documentation.

19950920 100

DTIC QUALITY INSPECTED 5

REPORT DOCUMENTATION PAGE			Form Approved OMB No. 0704-0188	
Public reporting burden for this collection of information is estimated to average 1 hour per response, including the time for reviewing instructions, searching existing data sources, gathering and maintaining the data needed, and completing and reviewing the collection of information. Send comments regarding this burden estimate or any other aspect of this collection of information, including suggestions for reducing this burden, to Washington Headquarters Services, Directorate for Information Operations and Reports, 1215 Jefferson Davis Highway, Suite 1204, Arlington, VA 22202-4302, and to the Office of Management and Budget, Paperwork Reduction Project (0704-0188), Washington, DC 20503.				
1. AGENCY USE ONLY (Leave blank)		2. REPORT DATE July 26, 1995		3. REPORT TYPE AND DATES COVERED Annual 1 Jul 94 - 30 Jun 95
4. TITLE AND SUBTITLE Development of Methods for Improved Breast Imaging Using Ultrasound			5. FUNDING NUMBERS DAMD17-94-J-4362	
6. AUTHOR(S) Dr. John M. Reid Dr. Athina P. Petropulu				
7. PERFORMING ORGANIZATION NAME(S) AND ADDRESS(ES) Drexel University Philadelphia, Pennsylvania 19104			8. PERFORMING ORGANIZATION REPORT NUMBER 02-00-35 #1	
9. SPONSORING/MONITORING AGENCY NAME(S) AND ADDRESS(ES) U.S. Army Medical Research and Materiel Command Fort Detrick, Maryland 21702-5012			10. SPONSORING/MONITORING AGENCY REPORT NUMBER	
11. SUPPLEMENTARY NOTES Major part of this report has been accepted for publication to the IEEE Trans on UFFC, 1995.				
12a. DISTRIBUTION/AVAILABILITY STATEMENT Approved for public release, distribution unlimited			12b. DISTRIBUTION CODE	
13. ABSTRACT (Maximum 200 words) A novel framework was introduced for the deconvolution of B-scan images. A model for the rf image was developed first, and then imaging distortions were reconstructed using higher-order statistics of the measured image lines. Based on the estimated distortions deconvolution of the corresponding image was performed, which for the case of images of tissue mimicking phantom as well as human tissue images, led to significant resolution improvement. In the past, estimation of distortions has been carried out using exclusively second order statistics (autocorrelation). Autocorrelation, however, can recover only the minimum phase equivalent of the true distortions, because it is blind to phase. Imaging distortions were also estimated using second order statistics of the image lines. It was demonstrated that although these estimates did lead to resolution improvement, the amount of improvement was far less significant than the one obtained with the higher-order statistics based estimates.				
DTIC QUALITY INSPECTED 5				
14. SUBJECT TERMS higher-order statistics, in-vivo distortion estimation, deconvolution, resolution improvement			15. NUMBER OF PAGES 49	
			16. PRICE CODE	
17. SECURITY CLASSIFICATION OF REPORT Unclassified	18. SECURITY CLASSIFICATION OF THIS PAGE Unclassified	19. SECURITY CLASSIFICATION OF ABSTRACT Unclassified	20. LIMITATION OF ABSTRACT Unlimited	

FOREWORD

Opinions, interpretations, conclusions and recommendations are those of the author and are not necessarily endorsed by the US Army.

Where copyrighted material is quoted, permission has been obtained to use such material.

Where material from documents designated for limited distribution is quoted, permission has been obtained to use the material.

Citations of commercial organizations and trade names in this report do not constitute an official Department of Army endorsement or approval of the products or services of these organizations.

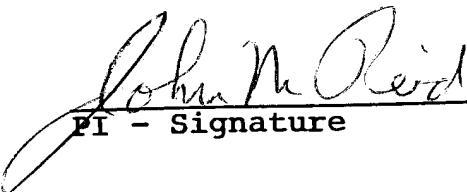
In conducting research using animals, the investigator(s) adhered to the "Guide for the Care and Use of Laboratory Animals," prepared by the Committee on Care and Use of Laboratory Animals of the Institute of Laboratory Resources, National Research Council (NIH Publication No. 86-23, Revised 1985).

For the protection of human subjects, the investigator(s) adhered to policies of applicable Federal Law 45 CFR 46.

In conducting research utilizing recombinant DNA technology, the investigator(s) adhered to current guidelines promulgated by the National Institutes of Health.

In the conduct of research utilizing recombinant DNA, the investigator(s) adhered to the NIH Guidelines for Research Involving Recombinant DNA Molecules.

In the conduct of research involving hazardous organisms, the investigator(s) adhered to the CDC-NIH Guide for Biosafety in Microbiological and Biomedical Laboratories.

 6/95
PI - Signature Date

Contents

FRONT COVER	1
REPORT DOCUMENTATION PAGE	2
FOREWORD	3
TABLE OF CONTENTS	4
5 INTRODUCTION	5
5.1 Nature of the problem	5
5.2 Background of previous work	6
5.3 Methods of approach	8
6 BODY	9
6.1 Modeling the rf image	9
6.1.1 In vivo distortion estimation using higher-order statistics (HOS) . .	11
6.1.2 In vivo estimation of the minimum phase equivalent of distortion using second-order statistics (SOS)	12
6.2 Experiments	13
6.3 Results	14
6.3.1 Water-tank experiments and the accuracy of our estimation method	14
6.3.2 HOS-based distortion estimation and the deconvolution of B-mode images	16
6.3.3 SOS-based estimated distortions and deconvolution of B-mode images	21
7 CONCLUSIONS/FUTURE WORK	21
8 REFERENCES	24
9 FIGURES/TABLES	28
10 PUBLICATIONS	44
11 PERSONNEL	50

Accession For	
NTIS CRA&I	<input checked="" type="checkbox"/>
DTIC TAB	<input type="checkbox"/>
Unannounced	<input type="checkbox"/>
Justification	
By	
Distribution /	
Availability Codes	
Dist	Avail and/or Special
A-1	

5 INTRODUCTION

5.1 Nature of the problem

The potential benefits of early diagnosis of cancer were recognized many years ago, before soft tissue imaging was available. This goal was behind the first efforts to apply ultrasound to the problem of the detection/diagnosis of breast cancer. Since then, many investigators have devoted effort to this problem because of the known advantages of ultrasound: it is non-ionizing, relatively inexpensive and uses widely available, portable, equipment. Today, with the success of x-ray mammography as an early screening tool, there is still room for improved methods, since there is disagreement regarding the use of ionizing radiation for screening, or routine exams. Also, the fibrous tissue of dense breasts gives poor results in conventional mammograms.

Ultrasound is now available as an adjunctive modality in many breast clinics, where it is used to determine if masses with smooth borders are cystic or solid and to examine dense young breasts. Biopsy is still used often to determine malignancy. The cystic/solid determination can be a problem in borderline cases, because of the tendency of some ultrasonic systems to "fill in" the echo free space with artifactual echoes and thus make a cyst appear to be solid. There is a need for better ultrasound systems, as well as to have a more general-purpose imaging modality available than the x-ray, particularly if this modality had the advantages listed for ultrasound.

Several factors have been identified in the literature as those contributing to poor resolution of ultrasound images. In B-Scan images, finite signal bandwidth of the ultrasonic transducers is a major reason for low resolution in the temporal axis, whereas the non negligible beam width highly contributes to that in the lateral direction [18], [7], [14], [44], [21]. The resolution also depends on the frequency at which the imaging system operates. In addition to equipment limitations, there are factors originating from the nature of the tissue being imaged. Phase aberrations and velocity variations arising from acoustic inhomogeneity of tissues are two of the important causes, not only for low resolution but also for low contrast in images [39], [11], [6]. The observed ultrasonic image can, therefore, be considered as a distorted version of the true tissue image, where the axial distortion is dominated by the pulse-echo wavelet of the imaging system and the lateral distortion by the lateral beam profile.

5.2 Background of previous work

The problem of compensating for imaging distortions has been very active research area, underscoring the importance in improving diagnostic quality of ultrasonic images. There have been several approaches to cancel out the aberration effects, but there is no consensus as to the best way to achieve it [10], [26], [25], [38]. In [10] it was proposed estimating the differences in arrival times between two adjacent receiving element locations using cross correlation techniques; these results were used to modify phasing characteristics of the transducers for ensuing scans. In [25], using an idea adapted from optics, phasing characteristics were determined using speckle brightness as a measure of image quality.

The availability of convolution models, such as in [17], [9], for ultrasound image formation and the wide availability of digital computers has given an added importance to discrete-time deconvolution methods, as a means of improving images beyond the capabilities of hardware. A few researchers have investigated the true 2-D deconvolution of RF images [9], [18], [32], whereas most of the published works are on 1-D techniques [44], [21], [23], [19], [14].

Since the resolution along the lateral direction was much worse than that along the temporal axis, a number of attempts were focussed on deconvolution of lateral image lines. In [44], a B-mode image was considered to be an ensemble of lateral lines corresponding to lateral slices through the envelope detected image, at given times (depth). Observing that the point-spread function of a typical pulse-echo imaging system is highly elongated along the lateral direction, they hypothesized that lateral image lines can be approximately described by a 1-D convolution model. Their model consisted of two 1-D terms: a signal of interest called the tissue reflectance and a blurring kernel in the lateral direction called the lateral point spread function. The latter function was defined to be the laterally varying component of the 2-D point spread function, whose axial variation had been approximated by a Dirac delta function. The problem of resolution enhancement was posed as one of extracting the the tissue reflectance from the observed image, assuming a *perfect knowledge* of the lateral point spread function. Using a Gaussian shaped hypothetical lateral point spread function, it was shown that at the best signal to noise ratio that can be expected from ultrasound images, deconvolution will lead to a resolution enhancement of no better than 2.0. The definition of the resolution was based on the reciprocal of the effective width of the lateral point spread function. However, the amount of improvement was also reported to be dependent on the exact shape of the lateral point spread function. These figures were found to be in agreement with the empirical numbers reported in [14]. Several others have reported results on 1-D lateral deconvolution [43], [33], [21], where in [33] it was concluded

that the computational effort on lateral deconvolution was wasted because of the very low resolution enhancement they could obtain at the expense of introducing more artifacts.

The drawbacks of the lateral deconvolution techniques discussed above are the following. Although the quantity displayed on an ultrasound imager is the envelope of the received RF signal, the image formation process actually occurs in the RF domain. In [32] it is pointed out that in general the convolutional model of image formation in the RF domain does not hold for envelope detected signals. It is concluded that the 1-D lateral deconvolution on envelope succeeds only in the special case where no phase interference from nearby reflectors is present.

All the papers, except [21], on lateral deconvolution mentioned above, relied on measuring the lateral beam profile to be used in computations. To obtain the true tissue image from the distorted observation, one requires quantitative information on the complex beam shape and acoustic velocity variations in-vivo, which are impossible to measure directly. In highly simplified situations such as measurements of wire targets under water, it is possible to get that information reliably. However, in the case of in-vivo tissue targets, such information is generally unavailable. The measurements done under water are not valid with clinical images, even when the imaging system used is the same, because of the effects of phase aberrations, nonlinearities and dispersive attenuation introduced by the tissues [21], [11], [39], [6], thus dramatically limiting the clinical applicability of those methods.

In [21], a line-by-line lateral deconvolution technique which does not require the complex beam shape in tissue or phase information on adjacent lateral lines, was proposed. This method too, however, worked on amplitude detected B-scan images. It hinges on the key assumption that the transfer function of the imaging system along a lateral image line can be approximated by the smoothed Fourier transform of the lateral image line itself. A convolution relationship between the envelope of a lateral point spread function and a slowly varying envelope of the tissue response has been tacitly assumed. Thus this method is subject to all the limitations implied by the above assumptions.

In spite of the fact that temporal resolution in an ultrasound image is much higher than the lateral resolution, axial deconvolution is still of importance. Besides the obvious advantage in improved axial resolution, the removal of the effect of the ultrasound pulse echo wavelet (through axial deconvolution) will tend to make the appearance of images more uniform over different subjects [16], thus simplifying the diagnosis procedures. As the shape of the pulse echo wavelet changes with propagation due to dispersive attenuation, a first step in axial deconvolution often involves the estimation of the pulse in tissue. Parametric modeling of speckle-only image lines has been proposed [37], [20], [16]. However, such approaches are limited by the problems such as the model order selection, associated with

parametric modeling. In [19] a Kalman filter technique was applied to estimate pulse echo wavelets as well as to simultaneously improve the axial resolution. The success of the method was reported to be dependent on the SNR of the observations and the accuracy at which the observations could be modeled. A non-parametric approach for the estimation of the pulse was proposed in [15], where the minimum-phase equivalent of the pulse-echo wavelet was separated from the tissue response. However, quite often pulse-echo wavelets and lateral kernels are non-minimum phase signals, thus limiting the generality of this approach.

5.3 Methods of approach

In the past year we introduced a novel non-parametric framework for deconvolution of B-scan images [1], [2], [3], [4], [5]. We first developed a model for the rf image, and then reconstructed distortions using higher-order statistics of the measured image lines. Based on the estimated distortions we performed deconvolution of the corresponding images and demonstrated that the resolution of ultrasound images of tissue mimicking phantom as well as human tissue images was significantly improved. In the past, estimation of distortions has been carried out using exclusively second order statistics (autocorrelation). Autocorrelation, however, can recover only the minimum phase equivalent of the true distortions, because it is blind to phase. We also estimated distortions using second order statistics of the image lines. We showed that although these estimates did lead to resolution improvement, the amount of improvement was less significant than the one obtained with the higher-order statistics based estimates.

Image formation process in the RF-domain is described by a 2-D convolutional model, where the attenuation of the pulse-echo wavelet and beam aberration effects can be indirectly incorporated [17], [18], [16]. Two 1-D blurring kernels, corresponding to axial and lateral directions, is hypothesized to represent distortions along respective axes. The axial distortion kernel includes the blurring effects due to the finite bandwidth of the transducer, and dispersive attenuation of the pulse-echo wavelet in tissue. The lateral distortion kernel represents the convolutional components of lateral blurring due to the complex beam patterns. Formalizing a definition for resolution, we show that compensation for the effects of the blurring kernels improves the resolution of the image.

The proposed method has the advantage of being able to estimate these kernels at each image line, axial and lateral, thus capturing the variations within the image. Since the estimations are based on higher-order statistics [24] of RF-data, the estimated kernels are robust to additive observation noise and also have correct phase. To the best of our

knowledge, the method we proposed [1] is the first one to in-vivo estimate the distortion kernels with their true phase, as opposed to conventional methods that estimate minimum-phase equivalent of kernels.

6 BODY

6.1 Modeling the rf image

During an ultrasonic investigation, a three-dimensional pulsed pressure field is emitted into the tissue. The field interacts with the tissue and part of it is reflected, scattered, and subsequently received by the transducer. Under the assumptions of linear propagation and weak scattering, an expression for the received pressure field was derived in [17], using the first order Born approximation. Absorption effects were neglected. The equation has been expressed as a convolutional model in the following form:

$$y(\mathbf{r}_2, t) = v_{pe}(t) *_t f(\mathbf{r}_1) *_r h_{pe}(\mathbf{r}_1, \mathbf{r}_2, t) + w(\mathbf{r}_2, t), \quad (1)$$

where:

- $\mathbf{r}_1, \mathbf{r}_2$ are vectors denoting the location of the scatterer and the transducer, respectively;
- “ $*_t$ ” and “ $*_r$ ” denote time and spatial convolution, respectively;
- $f(\mathbf{r}_1)$ originates from the inhomogeneities in the tissue due to density and propagation velocity perturbations above their mean levels, giving rise to the back scattered signal (*tissue response*);
- $v_{pe}(t)$ is the pulse-echo wavelet that accounts for the transducer excitation and the impulse responses during emission and reception of the pulse;
- $h_{pe}(\mathbf{r}_1, \mathbf{r}_2, t)$ is the modified pulse-echo spatial impulse response that relates the transducer geometry and the spatial extend of the scattered field. The computation of $h_{pe}(\mathbf{r}_1, \mathbf{r}_2, t)$ is based on the approach described in [41], [35]. Convolutional components of aberrations and dispersive attenuation, which introduce spatially varying effects to the process, may be incorporated in this already spatially varying kernel.
- $w(\mathbf{r}_2, t)$ represents measurement noise and the unmodeled dynamics of the image formation process.

The problem of extracting the tissue response $f(\mathbf{r}_1)$ from the observation $y(\mathbf{r}_2, t)$ is a deconvolution problem. Since a B-mode image is a mapping from the 3-D tissue space to the 2-D space of the display, the solution is not unique in general. This non-uniqueness should be obviated by making reasonable assumptions about the 3-D structure of the tissues being imaged [9]. An assumption implicit in cases where the deconvolution is done using

kernels confined to the imaging plane is that all image features in the imaging-plane extend perpendicular to the corresponding plane in the tissue space, so as to make the height of extension the effective height of the beam.

The convolution model of (17) expresses the fact that the received signal at the transducer site \mathbf{r}_2 is a result of linear spatio-temporal interaction between the signal of interest $f(\mathbf{r}_1)$ and a distortion kernel. Thus, the measured signal contains a distorted version of the true tissue response $f(\mathbf{r}_1)$. Deconvolving these kernels should improve image resolution and contrast. It should also remove aberration-induced artifacts that result from changing beam profiles inside the tissue.

As discussed in the introduction, efforts to carry out this deconvolution have been hampered by the difficulties in measuring the modified spatial impulse response of the imaging system. Underwater measurements using simplified targets would not reveal any significant changes undergone by the interrogating beam in tissue.

Our goal here is actually to identify the combination of $v_{pe}(t)$ and the spatially varying kernel $h_{pe}(\mathbf{r}_1, \mathbf{r}_2, t)$, and subsequently cancel it from the image in order to improve lateral as well as axial resolution. Let us combine both smoothing kernels $v_{pe}(t)$ and $h_{pe}(\mathbf{r}_1, \mathbf{r}_2, t)$ in one spatially and temporally varying kernel, $h(\mathbf{r}_1, \mathbf{r}_2, t)$, which we are going to refer to as the *ultrasonic system impulse response*. For discrete time, and for some fixed transducer location (17) is equivalent to the following two-dimensional convolutional model

$$y(l, n) = \sum_i \sum_j f(i, j) h(l - i, n - j) + w(l, n), \quad (2)$$

where $y(l, n)$ represents the sample from the l -th A-line at discrete time n . The goal here is to identify the time varying ultrasonic system response $h(l, n)$, and recover the tissue response, $f(i, j)$, from the noisy measurement $y(k, l)$.

However, we will not attempt a true 2-D deconvolution in this paper. As is commonly done in ultrasound deconvolution literature [15], [23], [18], [19], we assume that an RF A-line can be expressed as a convolution between two 1-D axial terms: a hypothetical tissue response and a distortion kernel. This view is not unique to the image deconvolution literature; ultrasound Doppler systems and tissue attenuation estimation techniques tacitly depend on it [15]. Reducing the problem to a 1-D deconvolution is analogous to the original decomposition of the true 3-D deconvolution problem in to a 2-D one.

6.1.1 In vivo distortion estimation using higher-order statistics (HOS)

In the following we will treat each image line (either in ateral or axial direction) separately assuming the 1-D model

$$y_i(n) = h_i(n) * f_i(n) + w_i(n), \quad i = 1, 2, \dots, \quad (3)$$

where i is the A-line index; $f_i(n)$ is the axial or lateral tissue response; $h_i(n)$ is the axial or lateral distortion kernel; which describes the distortion associated with the i -th line; and n denotes discrete time. We assumed that:

(A1) $h_i(n)$ is deterministic, possibly non-minimum phase,

(A2) $f_i(n)$ is stationary, white, independent identically distributed (i.i.d.), zero-mean non-Gaussian,

(A3) $w_i(n)$ is white zero-mean Gaussian, and independent of $f_i(n)$.

If we consider a region of the image that contains only speckle, these assumptions should hold reasonably well.

The third order cumulant of the observation $y_i(n)$ is defined as [24] :

$$c_{y_i}(\tau, \rho) = E\{y_i(n)y_i(n+\tau)y_i(n+\rho)\} \quad (4)$$

The bispectrum of the $y_i(n)$ is defined to be the Fourier transform of the third order cumulant. Under assumptions (A1) – (A3), the bispectrum of $y_i(n)$ is given by [24]:

$$C_{y_i}(\omega_1, \omega_2) = C_{f_i}(\omega_1, \omega_2)H_i(\omega_1)H_i(\omega_2)H_i^*(\omega_1 + \omega_2) + C_{w_i}(\omega_1, \omega_2) \quad (5)$$

where $C_{f_i}(\omega_1, \omega_2)$ is the bispectrum of $f_i(n)$, $H_i(\omega)$ is the spectrum of $h_i(n)$ and $C_{w_i}(\omega_1, \omega_2)$ is the noise bispectrum. If the additive noise is zero-mean Gaussian, then $C_{w_i}(\omega_1, \omega_2) = 0$ [24] and (4) becomes,

$$C_{y_i}(\omega_1, \omega_2) = C_{f_i}(\omega_1, \omega_2)H_i(\omega_1)H_i(\omega_2)H_i^*(\omega_1 + \omega_2) \quad (6)$$

The bicepstrum is defined as the cepstrum of the bispectrum, from which we get:

$$b_{y_i}(m_1, m_2) = b_{f_i}(m_1, m_2) + c_{h_i}(m_1, m_2), \quad (7)$$

where $b_{f_i}(m_1, m_2)$, $c_{h_i}(m_1, m_2)$ are the bicepstra of $f_i(n)$ and $h_i(n)$, respectively.

If $f_i(n)$ is stationary independent identically distributed (i.i.d.), its third order spectrum is flat and equal to the skewness, γ_{f_i} , of the process. Therefore, its bicepstrum will be an

impulse located at the origin. In that case, using bicepstral values along the main axes except at the origin, we can reconstruct a scaled and shifted version of $h_i(n)$ as:

$$h_i(n) = F^{-1}\{e^{F\{c_{h_i}(m)\}}\}, \quad (8)$$

where

$$c_{h_i}(m) = \begin{cases} b_{y_i}(m, 0) & m > 0 \\ 0 & m = 0 \\ b_{y_i}(-m, 0) & m < 0. \end{cases} \quad (9)$$

We assume that a similar 1-D model holds in the lateral direction of the RF-image. Then, a similar procedure can be followed to estimate lateral distortion kernels at each line. The kernels thus estimated will include the convolutional components of aberration as well. Therefore, axial deconvolution followed by lateral deconvolution, or various combinations thereof, should give us distortion compensated RF images which will have higher resolution and contrast. The ability to estimate and remove beam distortion effects (due to aberration) is seen as a major advantage of this method over other non-parametric techniques [15], [21]. The method proposed in [15], as is, can not estimate non-minimum phase signals, while that of [21] has been designed for envelope detected signals.

6.1.2 In vivo estimation of the minimum phase equivalent of distortion using second-order statistics (SOS)

Using the model of eq. (3), second order statistics were also used to estimate imaging distortions [12], [13].

Transforming (3) in the autocorrelation domain (second-order statistic) we get:

$$r_{y_i}(\tau) = E\{y_i(n)y_i(n+\tau)\} = \gamma_2^{f_i} \sum_n h_i(n)h_i(n+\tau) + \gamma_2^{w_i}\delta(\tau), \quad (10)$$

where $\gamma_2^{f_i}$ is the variance of $f_i(n)$, $\gamma_2^{w_i}$ is the variance of the noise, and $\delta(\tau)$ is the unit impulse. The power cepstrum is defined as the inverse Fourier transform of the logarithm of the Fourier transform of the autocorrelation. Assuming that the noise level is low enough, in the power cepstrum domain we get:

$$\hat{y}_i(k) \sim \hat{h}_i(k), \quad k \neq 0, \quad (11)$$

where $\hat{h}_i(k)$ is the power cepstrum of the distortion kernel associated with the i -th line. From its power cepstrum, we can reconstruct the minimum phase equivalent of $h_i(n)$ [27] as:

$$\hat{h}_i(n) = F^{-1}[\exp\{F[\hat{y}_i(k)w(k)]\}], \quad (12)$$

where $F[.]$ and $F^{-1}[.]$ denote forward and inverse Fourier transforms, and

$$w(k) = \begin{cases} 1, & k > 0 \\ 0, & \text{otherwise.} \end{cases} \quad (13)$$

6.2 Experiments

The goals of our experimental work were to:

1. Compare the axial distortions, estimated based on higher-order statistics (HOS-based distortions), with experimentally obtained ones. Validate the imposed assumptions (see Section 6.1.1).
2. Estimate HOS-based distortions from clinical ultrasound images. Deconvolve ultrasound images using the HOS-based estimated distortions. Quantify resolution improvement.
3. Deconvolve clinical image using distortions estimated based on second-order statistics (SOS-based distortions) as outlined in Section 6.1.2). Quantify resolution improvement.
4. Compare resolution improvement of deconvolution with HOS-based and SOS-based distortions.

Towards the above goals we collected the following data:

- Water-tank measurements:

Experiment A

We obtained B-Scan images of an ATS model 532 contrast resolution phantom which was positioned in a water tank. The target area consisted of the tissue mimicking background which had a scatterer density of 32 scatterers/ mm^3 . The transducer we used was a model GE104682 curved device with a nominal center frequency of 3.5 MHz. The nominal focal zone of the transducer was 6-13 cm. A stepper motor with a step size 0.025mm controlled the position of the transducer under the guidance of a personal computer. Data acquisition was done through a LeCroy model 9450A dual channel digital oscilloscope connected to the PC by a GPIB interface. Transducer was moved across the scanning plane in steps of 0.25mm, and RF echos were sampled at a 13.3 MHz rate.

Experiment B

A long piece of freshly peeled wire of diameter 0.812mm was placed underwater so that it was parallel to the transducer surface and perpendicular to the scanning plane. It was kept inside the focal zone of the transducer, at a distance 8cm away from the transducer surface. The experimental setup used here is the same as in *experiment (A)*. The wavelet reflected from the wire surface was recorded and taken to be an approximate estimate of the pulse-echo wavelet of the imaging system.

- Measurements from Clinical Equipment:

Experiment C

To demonstrate the performance of our method on data from more realistic equipment, we imaged the same ATS532 phantom using a linear array sector scan transducer on a model UltraMark-9 clinical imaging system manufactured by Advanced Technology Laboratories, Seattle, U.S.A. The target area consisted of two cylinders with scatterer densities 4 and 8 scatterers/ mm^3 , embedded in a tissue mimicking background of 32 scatterers/ mm^3 . The nominal center frequency of the scanner was 3.5 MHz; the field of vision was 60° . Data were sampled at a rate of 12 MHz. No TGC was employed.

Experiment D

To demonstrate the performance of our method under clinical conditions, we obtained a liver scan of a patient imaged by ultrasonologists at the Thomas Jefferson University Hospital, Philadelphia, on the same imaging system described under *experiment (C)*. The patient has been diagnosed with hypoechoic multiple liver metastatic tumor. No T.G.C. had been applied; focus of the imaging system at transmission was set at 2cm , and dynamic focusing was employed with the receiving mode.

6.3 Results

6.3.1 Water-tank experiments and the accuracy of our estimation method

In order to demonstrate the validity of our kernel estimation procedure, we used the data from underwater measurements, i.e. *experiments (A) and (B)*. A part of the RF image data that we gathered using the circular transducer in *experiment (A)* is shown in Fig. 1(a), where the logarithm of the envelope has been used for display purposes.

Under the assumption that the axial blurring kernel of an image line does not significantly depend on the lateral location of the line, data from several nearby axial RF lines can be used to make a longer data vector, which will enable us to obtain better cumulant estimates. In order to minimize the effect of attenuation on our estimations, from each A-line i we considered data segments $y_i(k)$ of length not more than $2N$ samples. The number of adjacent line segments $y_i(k)$ concatenated was in the range $i = 1 - 10$. In the axial kernel estimations, we used $M = 10$ and $N = 64$.

Axial blurring kernels estimated with the method of Section 6.1.1 from different regions of the image in Fig 1(a) are shown in Fig. 2(a), in dotted lines. All of these kernels have been estimated from axial data obtained at the *same depths* of the image, but at different lateral locations. The mean axial blurring kernel, $v_m(t)$, which was computed as the average of estimated kernels, is indicated by the solid line while the measured pulse echo wavelet is indicated by the dashed line.

It can be seen that all of the estimated kernels possess a similar structure, resembling a typical ultrasound pulse-echo wavelet. This is to be expected since the component due to the pulse-echo-wavelet ($v_{pe}(t)$) dominates the axial blurring kernel [18]. The variation among the estimated kernels may be attributed to the statistical estimation errors, deviation of the scatterer response from a statistically white response (which violates our assumption (A2)) and, contributions from the effects of the medium such as aberration and dispersive attenuation which have spatially varying characteristics.

There is a reasonable match between the measured and average estimated kernels (Fig. 2), *within the limits of the accuracy of the experimentation*. Looking at their spectra (see Fig. 2(b)) we can clearly see that the frequency spectrum of the estimated mean kernel has the salient features contained in the experimental pulse echo wavelet measured in *experiment (B)*. The center frequency of the spectra fall very close to the nominal center frequency of the transducer, 3.5 MHz. The measured wavelet has a slightly narrower main lobe, probably due to the ringing introduced by the wire target used in *experiment (B)*. However, it should be kept in mind that the measured kernel was obtained from simplified underwater experiments, which do not truly represent the situation inside the tissue mimicking phantom.

The differences between the average estimated kernel and the measured kernel can be attributed to:

- (E1) the variance associated with the estimation of third order cumulants,
- (E2) the much higher dispersive attenuation and aberrations encountered inside the phantom in *experiment (A)*, compared with those in *experiment (B)*,

(E3) the non-whiteness of the underlying scatter response of the phantom that violates assumption (A2),

(E4) approximate realization of a point target by a line target, in *experiment (B)*.

Averaging techniques that we used with both the cumulant estimates of observations and estimated kernels themselves, make the contributions to total error from (E1) small. The errors introduced by approximating a point target by a thin wire target does not introduce serious errors either; this method is being used in the testing of ultrasound transducers in research environments, [32], [21].

The major contribution to the differences in estimated and measured kernels are from (E2) and (E3). In fact, by virtue of modifying the frequency spectrum of the received signal, attenuations appear as one component contributing to the non-whiteness (color) of the scatterer response, and thereby affects the kernel estimation procedure. To minimize the effect of attenuations on the stationarity of our observations, we considered only short segments (eg. 64 or 128 samples at a 13.3MHz sampling rate) from each A-line of interest. Identifying and compensating for the color of the tissue response can be achieved by applying the blind deconvolution procedure proposed in [31] on different image lines [2].

The results we obtained support our model assumptions (A1)–(A3). It should be noted that (A2) actually contradicts the Gaussianity assumption, which is commonly made for the tissue response. However, non Gaussian models for the backscattered ultrasonic signals have been suggested and used in the past [42], [34], [29], [30]. In the method proposed here, if the tissue response were Gaussian, it would have been suppressed in the bispectrum domain, thereby rendering the estimation of an axial blurring kernel an impossibility. Hence, our success in the estimation supports the non Gaussianity assumption for RF ultrasound data. The structure of the measured kernel (*experiment (B)*) suggest that the axial kernel is indeed a non-minimum phase signal; the method proposed in this paper is capable of estimating non-minimum phase signals in contrast to existing techniques which can only estimate the minimum-phase equivalent of the true non-minimum phase signal.

We consider the agreement between the estimated and measured kernels satisfactory *within the ability of underwater measurements (Measurement B) to match the situation inside the phantom.*

6.3.2 HOS-based distortion estimation and the deconvolution of B-mode images

Images of a tissue mimicking phantom obtained with a single element transducer.

Having established the validity of our assumptions and the kernel estimation technique

in the axial direction, we proceeded to estimate lateral distortion kernels from the image obtained in *experiment (A)*, and to perform deconvolution. The lateral distortion kernels we estimated at locations covering a range of depths 6.58cm - 9.42cm from the transducer surface can be seen in Fig. 3(a); their spectra are shown in Fig. 3(b). In these estimations, we used $N = 32$ and $M = 10$. Five adjacent lateral lines were used in each kernel estimation.

In the lateral direction, the estimated kernels have characteristics similar to the lateral beam profiles of the imaging system. Unfortunately, there is no direct way to verify the results of our lateral estimations. In conventional transverse beam profile estimations, the experiments are usually done under water, and the pressure profiles are peak detected. This process masks instantaneous features of the beam, hence the results of such experiments can not be used in a verification. Moreover, it has been shown that in the presence of aberration, the lateral point spread function may undergo significant modifications [6], [39], possibly serious enough to change diagnoses in clinical situations [39]. Time histories of two dimensional instantaneous beam profiles at the focus, shown in [22], are in agreement with the observation that the lateral beam profile can depart heavily from the ideal in the presence of tissue inhomogeneities. These results suggest that, in principle, underwater experiments or theoretical formulae that do not take aberration in to account, can not be used in verifying lateral blurring kernels estimated from complex targets. Further, it should be noted that even though our lateral kernels are estimated at individual lateral image lines (i.e., at a fixed time) nearby lines contribute to the data at a given time by virtue of the spatio-temporal nature of Ultrasonic System Impulse Response defined earlier.

Once the distortion kernels have been identified, retrieving the corresponding true tissue response becomes a typical deconvolution process. For the deconvolution, we used the constrained Wiener filter technique described in [40]. In performing the axial deconvolution, we used the mean HOS-based axial distortion kernel, $v_m(t)$ shown in Fig. 2., which was obtained with the method of Section 6.1.1; in the lateral direction, the mean lateral distortion kernel obtained as the average of the estimated kernels shown in Fig. 3 was used.

Fig. 1(b) shows the logarithmically compressed envelope of the B-scan image, derived from the laterally deconvolved RF data corresponding to the original image shown in Fig. 1(a). The axially deconvolved image is in Fig. 1(c) and the laterally followed by axially deconvolved image is in Fig. 1(d). Each image represents an area of $2.5\text{cm} \times 2.0\text{cm}$ in the true tissue space. For the sake of computational simplicity, we assumed that the lateral (and axial) blurring kernel do not vary significantly over different RF-image lines or different image depths in the amounts we are concerned with here. This allowed us to use a single blurring kernel, in each of the axial and lateral directions, to deconvolve the entire image. Using the average lateral kernel to laterally deconvolve a region of the image is justifiable

by the fact that all the kernels estimated from the depth range covering the image shown here (6.58cm to 9.42cm) show a certain degree of similarity. This may be due to the fact that the transducer we used had a focal zone of 6-13cm, into which range the lateral image lines considered above belong. Moreover, the phantom we used in experiments had not been designed to simulate strong aberrating effects. As for the axial deconvolutions, the pulse echo wavelet (the major contributor to the axial distortion kernel) of the imaging system is known to stay fairly constant over different RF-lines across the image [18], [16]; our results shown in Fig. 2 also support that hypothesis. However, the method proposed here is still valid, if one needs to estimate kernels for localized regions or individual image lines. To capture fine details in the pass band of the spectrum, one may still require a line by line, or region by region, lateral deconvolution.

Quantifying resolution improvement

According to Fig. 1, the deconvolution in the RF-domain results in a significant reduction in the size of speckles, suggesting a gain in resolution. In order to quantify the apparent increase in resolution, we defined a measure of resolution based on the 2-D auto-covariance function of the image. Auto-covariance function of an image was computed on the *RF data* corresponding to the image, with the peak value of autocovariance normalized to 1.0. The lateral slice, L_{00} , through the peak of the 2-D auto-covariance function was considered in defining the *lateral resolution*. The axial slice, A_{00} , through the peak in defining the *axial resolution*. Similarly, the lateral resolution, $R_d^{(l)}$, was defined as the reciprocal of the width of L_{00} , at d dB below the peak of the slice. Axial resolution was defined similarly except for the fact that the envelope of the absolute value of the slice A_{00} was used. In this paper we used $d = 5.00$ and $d = 10.00$. Defining the resolution at two different *dB* levels allows us to get a better idea of the shape of the auto-covariance function.

The reason for defining the axial resolution based on the envelope of absolute value of A_{00} is as follows. We define the resolution in terms of the width, l_0 , of the *main lobe* of the auto-covariance function because, l_0 is a measure of the average “smallness” of the basic building elements of the image. In the axial direction, the representation of a point target is an oscillatory, time-limited signal. Therefore, even when the target is a point in space, the received signal would have an auto-covariance function which shows oscillatory behavior (eg. Fig. 4(d)). In this case, the central lobe conveying information on the average image element size is the envelope of the absolute value of the auto-covariance function.

The resolution was defined in the RF domain, because our kernel estimation and deconvolution procedure was done entirely in the RF-domain. The process of envelope detecting itself introduces blurring leading to an inaccurate estimate of the potential resolution deliv-

ered by deconvolution, thus making the envelope detected signal domain a less than ideal place to define resolution. Fig. 4(a) shows a 2D shaded mesh plot of the auto-covariance function of the RF-data corresponding to original image in Fig. 1(a). Fig. 4(b) shows the auto-variance function after lateral and axial deconvolutions. Absolute values of the auto-covariance function have been plotted for easy visualization. The slice L_{00} is shown in Fig. 4(c), where the solid line indicates the slice corresponding to the original image (Fig. 1(a)) and the dotted line that of the laterally and axially deconvolved image (Fig. 1(c)). Corresponding plots of the axial slice A_{00} are in Fig. 4(d).

The general decrease, in all directions, of the width of the main-lobe of the auto-covariance function due to deconvolution is obvious from Figs. 4(a) and 4(b). From Fig. 4(c), we computed the *lateral resolution gain*, G_d^l , defined as:

$$G_d^{(l)} = \frac{R_d^{(l_o)}}{R_d^{(l_d)}}, \quad d = 5dB, 10dB, \quad (14)$$

where $R_d^{(l_o)}$ and $R_d^{(l_d)}$ respectively represent lateral resolutions before and after deconvolution. A similar definition holds for the *axial resolution gain*. The lateral resolution gain at $d = 5dB$ and $d = 10dB$ levels, between the original (Fig. 4(a)) and the laterally followed by axially deconvolved image (Fig. 4(c)) was found to be 2.7 and 3.0 respectively. The corresponding figures for axial resolution gain, $G_d^{(a)}$, was 1.73 and 1.72 respectively.

Our results indicate that the lateral resolution gain is higher than the axial resolution gain. Coupled with the fact that, in the original image blurring was much higher in the lateral direction, we can conclude lateral deconvolution is mostly responsible for the improvement in overall resolution.

To investigate the effects of deconvolution on “speckle noise” levels, we defined the signal-to-noise ratio as, $SNR = (\frac{\mu}{\sigma})$, where μ is the mean of the image and σ^2 is the variance. Since we performed our deconvolutions in the RF domain, our SNR calculations were also done in the RF-domain, on absolute values of RF-data. Computed over the original image (Fig. 1(a)), $SNR = 1.24$; computed over the laterally and axially deconvolved image, $SNR = 1.26$. After only an axial deconvolution. (Fig. 1(c)), $SNR = 1.25$, and after only a lateral deconvolution (Fig. 1(b)), $SNR = 1.23$. Based on these numbers, we conclude that the deconvolution results in a gain in resolution, but does not significantly alter speckle noise levels. The results of SNR computations and resolution gains have been summarized in Tables 1 and 2.

Images of a tissue mimicking phantom obtained with clinical equipment

In order to investigate the performance of our technique with B-scan images taken from

modern clinical equipment, we estimated axial and lateral distortion kernels from the RF-data collected in *experiment (C)*. Fig. 5(a) shows the logarithmically compressed envelope of the original B-scan image. Average axial and lateral kernels estimated from the RF-data corresponding to Fig. 5(a) are illustrated in Fig. 6(a) and 6(b) respectively. These kernels indicate the average of 20 kernels estimated from the tissue mimicking background region of the phantom, between the two target cylinders (see Fig. 5). The spectra of the average axial kernel is shown in Fig. 6(c) and that of the average lateral kernel in Fig. 6(d).

The result of lateral deconvolution is shown in Fig. 5(b); the result of lateral followed by axial deconvolution is shown in Fig. 5(c). Average estimated kernels shown in Fig. 6 were used in both axial and lateral deconvolutions. Clearly, the deconvolution has resulted in a reduced speckle size and cleaner, better defined boundaries of the target cylinders. It is also evident that the attenuations associated with the imaging process show up much clearly in the deconvolved image. This may have significance in clinical imaging situations, where attenuation properties of tissue convey important diagnostic information.

Fig. 7(a) and 7(b) illustrate the absolute value of the auto-covariance function of the RF-data corresponding to the original (Fig. 7(a)) image and the laterally and axially deconvolved image (Fig. 7(d)), respectively. Fig. 7(c) and 7(d) show the lateral and axial slices L_{00} and A_{00} used to compute resolution gains. Based on data corresponding to Figs. 5 and 7, speckle SNR and resolution gains were computed and tabulated in Tables 1 and 2. Figs. 5, 7 and Tables 1 and 2 lead to the conclusion that considerable resolution enhancement is possible with deconvolution, and that the process of deconvolution does not affect the speckle noise significantly. Once again, lateral resolution is found to be mostly responsible for the overall improvement in the image.

Clinical images of a human liver

To evaluate our method with clinical images, we obtained a B-scan of a liver image as described in *experiment (D)*, section 3.1. Figure 8(a) shows a part of the logarithmically compressed envelope of the original image. Fig 9(a) and 9(b) show the average axial and lateral distortions estimated from the RF-data corresponding to Fig. 8(a). Their spectra can be seen in Figs. 9(c) and 9(d).

The results of lateral deconvolution is shown in Fig. 8(b); results of lateral followed by axial is in Fig. 8(c). In all cases, logarithmically compressed envelope of the images has been displayed.

Again, to visualize the improvement in resolution, we plotted the auto-covariances of the original and deconvolved images. Fig. 10(a) and 10(b) illustrates the shaded 2-D mesh plot of the auto-covariances of RF-data corresponding to Figs. 8(a) and 8(c) respectively.

Corresponding L_{00} and A_{00} slices are shown in Figs. 10(c) and 10(d). Slices corresponding to original image are shown in solid lines, whereas those of the deconvolved image are shown in dotted lines.

The lateral resolution gain, $G_d^{(a)}$ at $d = 5dB$ and $d = 10dB$ was found to be 3.0 and 2.5 respectively. Corresponding numbers for the axial resolution gain were 1.7 and 1.5. Speckle SNR ratio computed for the original image (Fig. 8(a)) was $SNR = 1.20$; after lateral and axial deconvolutions (Fig. 8(c)) $SNR = 1.33$. Tables 1 and 2 summarize these results.

These results suggest that considerable gain in resolution is possible with axial and lateral deconvolution of clinical images.

6.3.3 SOS-based estimated distortions and deconvolution of B-mode images

From the images obtained at experiments A, C and D, SOS-based distortions were estimated with the method of Section 6.1.2. The images were subsequently deconvolved, and the deconvolution results are shown in Figs. 11, 12 and 13, respectively. The corresponding resolution gains and speckle SNR are shown in Tables 3 and 4.

Comparing Tables 1 and 2 to 3 and 4, we can conclude that the resolution improvement, both axial and lateral, was consistently superior when deconvolution was performed with the HOS-based estimated distortions. Deconvolution with HOS-based estimates led to axial resolution improvement 1.15 - 1.9 times higher than deconvolution with SOS-based estimates. The improvement of lateral resolution when deconvolving using HOS based estimates was more dramatic; it was better than the SOS based deconvolution by a factor in the range 1.68-4.5. The superiority of the HOS-based deconvolution is also evident by comparing the corresponding images deconvolved with HOS and SOS-based distortion estimates.

7 CONCLUSIONS/FUTURE WORK

Processing ultrasound images with higher-order spectral operations we were able to identify the distortion introduced by the ultrasonic system and the medium. The proposed method makes it possible to estimate both axial and instantaneous lateral blurring kernels, working on B-mode RF data. Distortion identification and subsequent cancelling (deconvolution) operations were carried out on 1-D lines of the RF image, thereby obviating the theoretical difficulties faced by earlier attempts at beam deconvolution on envelope detected images. The method is capable of estimating mixed phase distortion kernels, and is immune to additive Gaussian noise.

Performing underwater experiments employing single element transducers, commercial tissue mimicking phantoms and simulated point targets, we showed that our kernel estimation procedure could be done with reasonable accuracy. The accuracy of the estimations were verified by measuring axial kernels underwater.

Deconvolution results obtained with phantom data and clinical images indicate considerable resolution improvement. Lateral deconvolution contributes heavily to the gain in resolution, where the resolution was defined in terms of the dimensions of the autocovariance function of the image. These results are significant because in unprocessed images, lateral distortions are known to be as much as 3-5 times severe than axial distortions, leading to a change in appearance in clinical images depending on the orientation of the scanner. Through lateral deconvolution, one can compensate for the lateral distortions and try to achieve consistent images independent from the angular position of the scanner. In the past, distortion estimation was carried out exclusively in the second-order statistics domain. We demonstrated that deconvolution based on HOS-based distortion estimates leads to superior axial and in particular lateral resolution improvement than the one with SOS-based estimates.

It has been reported that high transducer frequencies required for high resolution imaging actually lead to lower resolution in the presence of increased aberration in breast at higher frequencies [8]. In [36] it is pointed out that medium inhomogeneities are also important in systems where a larger aperture is used for higher lateral resolution. In general, the aberration correction is of fundamental importance in high resolution medical ultrasonic systems. The ability of the proposed method to compensate for convolution components of aberration holds promise in improving the diagnostic value of B-mode medical images beyond the capabilities of hardware.

Deconvolution, viewed as an image de-blurring/restoration operation, should reveal those small structures (such as early stage tumors) that had been hidden away from view due to imaging distortions (including convolutional components of aberrations), but otherwise would show up *on a hypothetical, perfect imager*. A deconvolved image also means access to a distortion-free tissue signal, which is largely independent of the imaging system. Therefore, tissue characterization schemes which ideally require imaging-system-independent data could be based on deconvolved RF images. In addition, the estimated distortion kernels themselves carry information on the statistical structure of scatterer field as manifested through the color of the scatterer response (tissue response), attenuations and, propagation non-linearities associated with the phantom (tissue).

Currently, efforts are under way to see how much improvement in resolution is possible with ultrasound images of the breast. We have ordered a custom made anthropomorphic

breast phantom and we we expect to begin experiments with breast data within August 1995.

8 REFERENCES

References

- [1] U.R. Abeyratne, A.P. Petropulu and J.M. Reid, "Higher Order Spectra Based Deconvolution of Ultrasound Images," *IEEE Transactions on UFFC*, to appear in 1995.
- [2] U.R. Abeyratne, A.P. Petropulu and J.M. Reid, "On Modeling the Tissue Response From Ultrasonic B-Scan Images," *IEEE Transactions on Medical Imaging*, submitted in February 1995.
- [3] U.R. Abeyratne, A.P. Petropulu and J.M. Reid, "Blind Deconvolution of Ultrasound Images," *SPIE International Symposium on Optics, Imaging and Instrumentation*, San Diego, July 1994.
- [4] U.R. Abeyratne, A.P. Petropulu, J.M. Reid and T. Golas, "Estimating Imaging Distortions and Tissue Response From Ultrasonic Images," *20th International Symposium on Ultrasonic Imaging and Tissue Characterization*, Arlington, VA, June 1995.
- [5] U.R. Abeyratne, A.P. Petropulu and J.M. Reid, "Higher Order Spectra Based Deconvolution of Ultrasound Images," *IEEE Workshop on Nonlinear Signal and Image Processing*, Neos Marmaras, Greece, June 1995.
- [6] V. N. Adrov and V. Chernomordik, "Mathematical Simulation of Pressure Pulse Propagation in Biological Tissue", *Ultrasonic Imaging*, Vol. 15, pp 59-71, 1993.
- [7] F. Arditi, S. Foster and J. W. Hunt, "Transient Fields of Concave Annular Arrays", *Ultrasonic Imaging*, 3, pp 37-61, 1981.
- [8] W. J. Davros, E. L. Madsen and J. A. Zagzebski, "Breast Mass Detection by US: a phantom study," *Radiology*, 156, pp 773-775, 1985.
- [9] M. Fatemi and A. C. Kak, "Ultrasonic B-Scan Imaging: Theory of Image Formation and a Technique for Restoration", *Ultrasonic Imaging*, Vol. 2, pp 1-47, 1980.
- [10] S. W. Flax and M. O'Donnell, "Phase aberration correction using signals from point reflectors and diffuse scatterers: Basic principles", *IEEE Trans. Ultr., Ferroelec., Freq. Contr.*, V UFFC-35, pp. 758-767, 1988.

- [11] P. D. Freiburger, D. C. Sullivan, B. H. LeBlanc, S. W. Smith, G. E. Trahey, "Two Dimensional Ultrasound Beam Distortion in the Breast: In Vivo Measurements and Effects.", *Ultrasonic Imaging*, Vol 14, pp 398 -414, 1992.
- [12] T. Golas, A.P. Petropulu, J.M. Reid, "In-vivo distortion estimation from ultrasound images: a comparative study of autocorrelation based versus higher-order statistics based methods," *Intern. Conf. on Acoustics Speech and Signal Processing*, ICASSP-96, Atlanta GA, 1996, submitted.
- [13] T. Golas, A.P. Petropulu, J.M. Reid, "In-vivo distortion estimation from ultrasound images: a comparative study of autocorrelation based versus higher-order statistics based methods," to be submitted to the *IEEE Trans. on UFFC*.
- [14] E. E. Hundt, E. A. Trautenberg, "Digital Processing of Ultrasound Data by Deconvolution", *IEEE Transactions on Sonics and Ultrasonics* , Vol. SU-27, No. 5, pp 249-252, 1980.
- [15] J. A. Jensen and S. Leeman, "Nonparametric Estimation of Ultrasound Pulses", *IEEE Trans. Biomedical Engineering* , Vol. 41, No. 10, pp 929-936, October 1994.
- [16] J. A. Jensen, "Estimation of Pulses in Ultrasound B-Scan Images", *IEEE Trans. on Medical Imaging* . MI-10, NO. 2, pp 164-172, 1991.
- [17] J. A. Jensen, "A model for the propagation and scattering of ultrasound in tissue", *J. Acoust. Soc. Amer.*, 89, pp. 188-191, 1991.
- [18] J. A. Jensen, "Deconvolution of Ultrasound Images", *Ultrasonic Imaging*, V14, pp.1-15 1992.
- [19] R. Kuc, "Application of Kalman Filtering Techniques to Diagnostic Ultrasound ", *Ultrasonic Imaging*, Vol. 1, pp 105-120, 1979.
- [20] R. Kuc and H. Li, "Reduced Order Autoregressive Modeling for Center Frequency Estimation", *Ultrasonic Imaging*, Vol. 7, pp 244-251, 1985.
- [21] C. N. Liu, M. Fatemi and R. C. Waag. "Digital Processing for Improvement of Ultrasonic Abdominal Images". *IEEE Trans. on Medical Imaging*. MI-2, NO. 2, pp 66-75, 1983.
- [22] D. -L. Liu and R. C. Waag. "Time-shift Compensation of Ultrasonic Focus Degradation Using Least-Mean-Square Error Estimates of Arrival Time" *J. of Acoust. Soc. Am.* 95(1), pp 542-555. 1994.

- [23] X. M. Lu, "L1 and L2 norm deconvolution and its application in medical ultrasound", *Ph.D. dissertation*, Drexel University, 1992.
- [24] C. L. Nikias and A.P. Petropulu, **Higher-Order Spectra Analysis: A Nonlinear Signal Processing Framework**, Prentice Hall Incorporated, Oppenheim Series in Signal Processing, 1993.
- [25] L. Nock, G.E. Trahey and S.W. Smith, "Phase aberration correction in medical imaging using speckle brightness as a quality factor", *J. Acoust. Soc. Amer.*, v 85 pp. 1819-1833, 1988.
- [26] M. O'Donnell and W.E. Engeler, "Real-time phase aberration correction system for medical ultrasound imaging", *Proc. IEEE 1990 Engr. in Med. and Biol. Meeting*, pp. 278-280, 1990.
- [27] A. V. Oppenheim, R. W. Schaffer, **Discrete-Time Signal Processing**, Englewood Cliffs, NJ: Prentice-Hall, 1989.
- [28] A. Papoulis and C. Chamzas, "Improvement in Range Resolution by Spectral Extrapolation", *Ultrasonic Imaging*, Vol. 1, pp 121-132, 1979.
- [29] A. P. Petropulu, "Higher order spectra in biomedical signal processing", *CRC Press Biomedical Engineering Handbook*, 1995.
- [30] A. P. Petropulu, "Higher order spectra in biomedical signal processing", *International Federation of Automatic Control (IFAC) Biomedical Symposium*, Galveston, Texas, March 27, 1994.
- [31] A. P. Petropulu and C. L. Nikias, "Blind Deconvolution Using Signal Reconstruction from Partial Higher Order Cepstral Information", *IEEE Transactions on Signal Processing*, Vol. 41, No. 6, pp 2088-2095, 1993.
- [32] D. E. Robinson and M. Wing, "Lateral Deconvolution of Ultrasound Beams", *Ultrasonic Imaging*, 6, pp. 1-12, 1984.
- [33] H. Schomberg, W. Vollmann and G. Mahne, "Lateral Inverse Filtering of Ultrasonic B-Scan Images", *Ultrasonic Imaging*, Vol. 5, pp 38-54, 1983.
- [34] P. M. Shankar, J. M. Reid, H. Ortega, C. W. Piccoli and B. B. Goldberg, "Use of Non-Rayleigh Statistics for the Identification of Tumors in Ultrasonic B-Scans of the Breast", *IEEE Transactions on Medical Imaging*, Vol. 12, pp 687-692, 1993.

- [35] P. R. Stepanishen, "The time-dependent force and radiation impedance on a piston in a rigid infinite planar baffle", *J. Acoust. Soc. Am.*, v. 49, pp. 841-849, 1971.
- [36] Y. Sumino and R. C. Waag, "Measurement of Ultrasonic Pulse Arrival Time Differences Produced by Abdominal Wall Specimens", *J. Acoust. Soc. Am.*, 90(6), 2924-2930, 1991.
- [37] C. W. Towfig, C. W. Barnes and A. J. Pisa, "Tissue Classification based on Autoregressive Models for Ultrasound Pulse Echo Data ", *Acta Electronica*, Vol 26, pp. 95-110, 1984.
- [38] G. E. Trahey, D. Zhao, J. A. Miglin and S. W. Smith, "Experimental Results with a real-time Adaptive Ultrasonic Imaging System for Viewing Through Distorting Media", *IEEE Tr. on Ultr. Ferroelec. and Frequency Control* , Vol. 37, pp 418-427, 1990.
- [39] G. E. Trahey, P. D. Freiburger, L. F. Nock and D. C. Sullivan, "In-vivo Measurements of Ultrasonic Beam Distortions in the Breast.", *Ultrasonic Imaging*, Vol 13, pp 71-90, 1991.
- [40] S. Treitel and L.R. Lines, "Linear inverse theory and deconvolution," *Geophysics*, vol. 47(8), pp. 1153-1159, August 1982.
- [41] G. E. Tupholme, "Generation of acoustic pulses by baffled pistons", *Mathematica*, v. 16, pp. 209-224, 1969.
- [42] R. H. Tuthill, R. H. Sperry and K. J. Parker, "Deviations From Rayleigh Statistics in Ultrasound Speckle", *Ultrasonic Imaging*, 10, pp 81-89, 1988.
- [43] R. Vaknine and W. J. Lorenz, "Lateral Filtering of Medical Ultrasonic B-Scans Before Image Generation", *Ultrasonic Imaging*, Vol. 6, pp 152-158, 1984.
- [44] W. Vollmann, "Resolution Enhancement of Ultrasonic B-Scan Images by Deconvolution", *IEEE Transactions on Sonics and Ultrasonics* , Vol. SU-29, NO. 2, pp 78-83, 1982.

9 FIGURES/TABLES

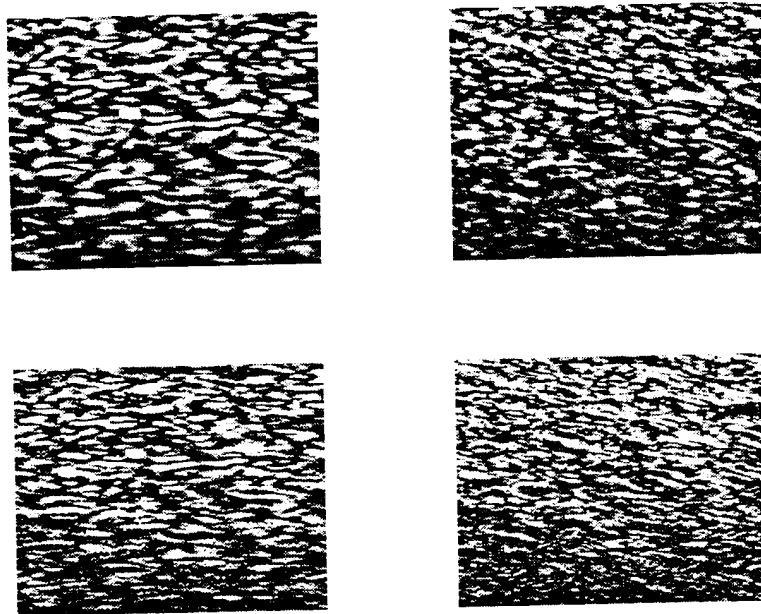


Fig.1 A speckle-only part of the ultrasound image of the tissue mimicking phantom, obtained with a focused single element transducer *experiment* (A); (b) the result of lateral deconvolution; (c) the result of axial deconvolution and, (d) the result of lateral followed by axial deconvolution. In all cases, the logarithmically compressed envelope is shown. Deconvolution was performed with the **higher-order statistics** based estimated distortions.

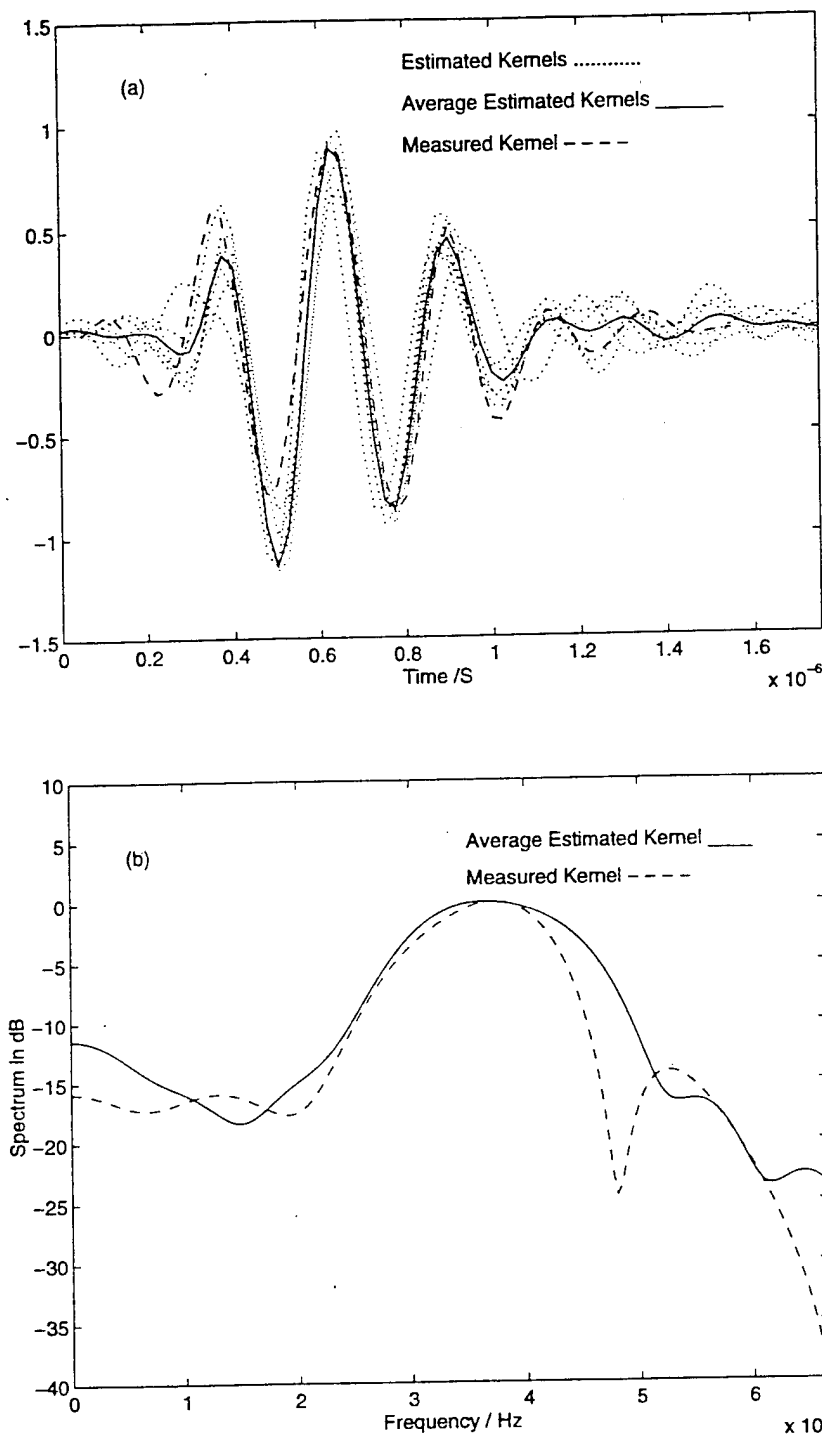


Fig.2 Underwater experiments (*experiments (A) and (B)*): (a) axial kernels estimated at various lateral positions in the B-mode image of the tissue mimicking phantom (dotted lines); average of the estimated kernels (solid line). The experimental kernel, measured as the reflection off a 0.812mm diameter wire surface, under water. The close agreement between the estimated and the measured kernels (with in limits of experimental errors), indicates the success of the estimation procedure. (b) Spectra of the average estimated kernel (solid line) and the measured kernel (dashed line). The center frequency of both kernels are compatible with the nominal center frequency of the transducer, 3.5MHz .

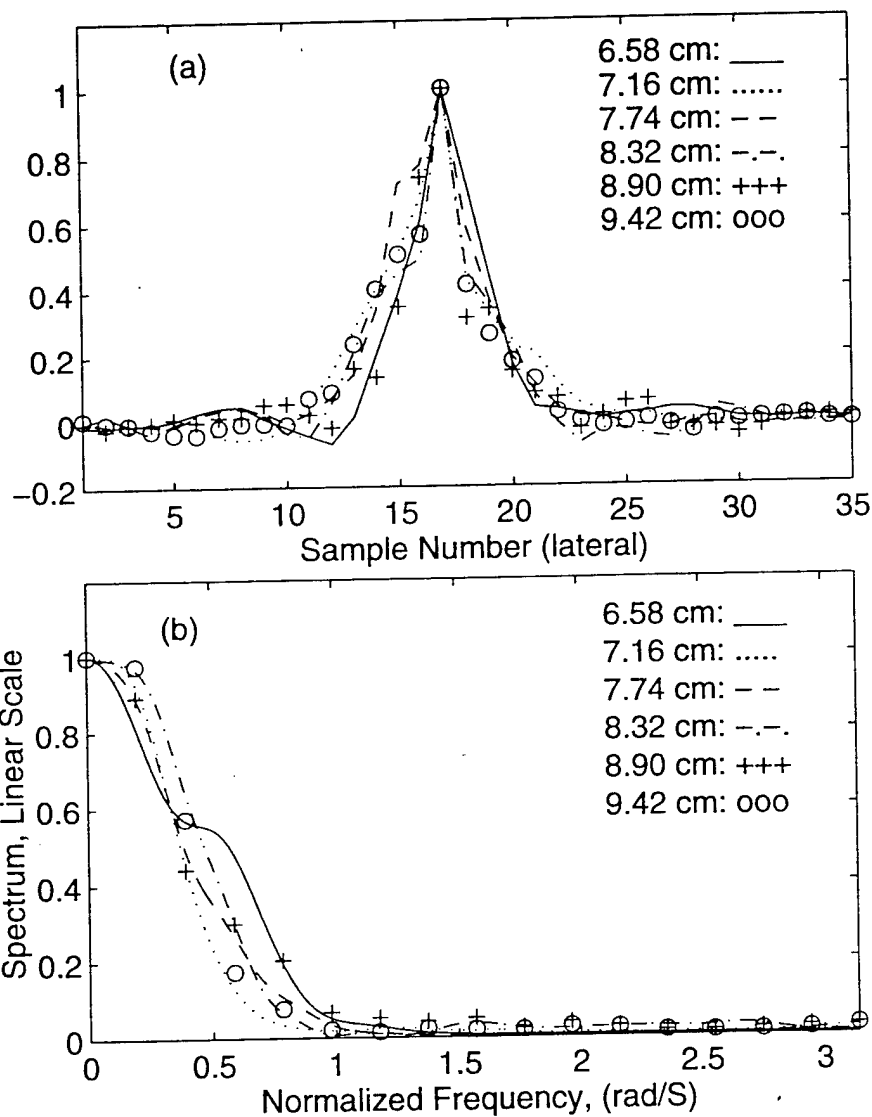


Fig.3 (a) Lateral distortion kernels estimated at various axial depths from the RF data corresponding to the image shown in Fig. 1(a). All the kernels are estimated within the focal zone of the transducer, 6 – 13cm. (b) Spectra of the lateral kernels shown in (a).

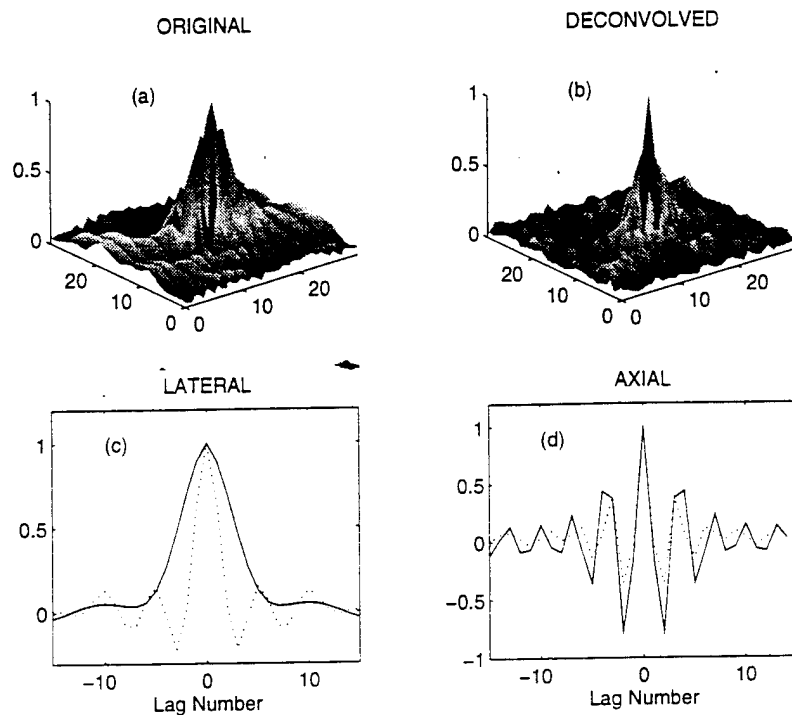
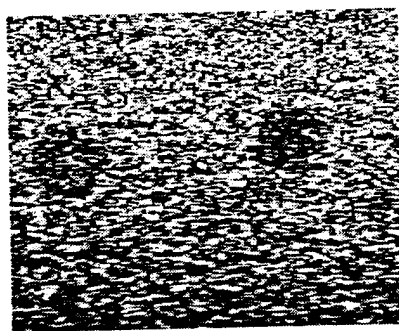
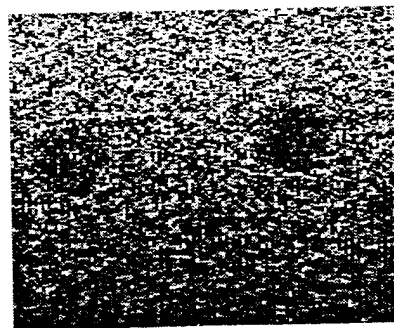


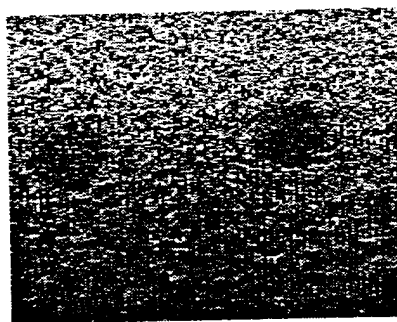
Fig.4 Shaded auto-covariance function of the RF-data corresponding to: (a) the original image shown in Fig. 1(a); (b) the laterally and axially deconvolved image shown in Fig. 1(d). Absolute values of the auto-covariance functions have been shown for easy visualization. (c) The lateral slice L_{00} and (d) the axial slice A_{00} of the auto-covariance function corresponding to: the original image (solid lines), the deconvolved image (dotted lines).



(a)



(b)



(c)

Fig.5 (*Experiment (C)*): (a) The original image of the tissue mimicking phantom obtained with the linear array transducer on a clinical imaging system; (b) the result of lateral deconvolution and (c) the result of lateral and axial deconvolution. The logarithmically compressed envelope has been used for display. Deconvolution was performed with the **higher-order statistics** based estimated distortions.

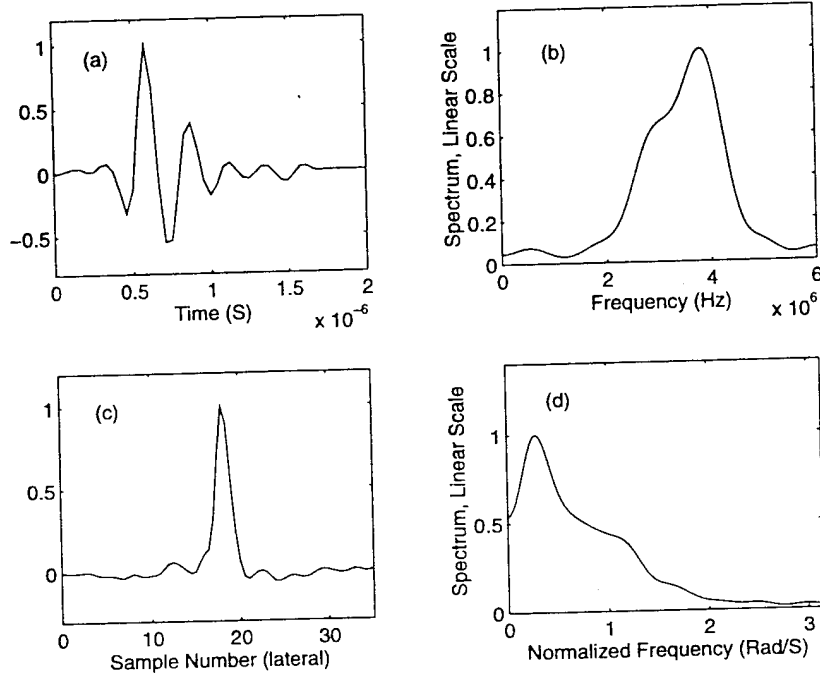


Fig.6 (*Experiment (C)*): (a) The average of the estimated axial kernels from RF-data corresponding to image shown in Fig. 5(a), and (b) its spectrum. (c) The average of the lateral kernels estimated from RF-data corresponding to Fig. 5(a) and (d) its spectrum. These kernels were estimated from the region between the two cylindrical targets in Fig. 5(a).

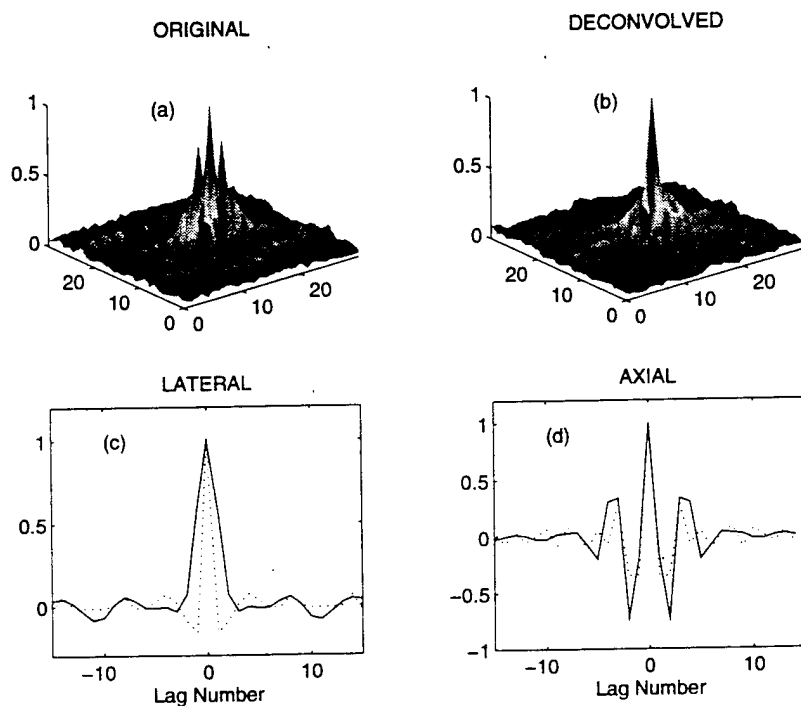
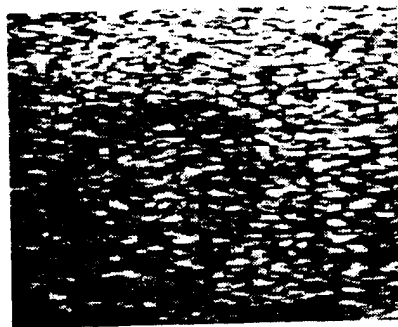
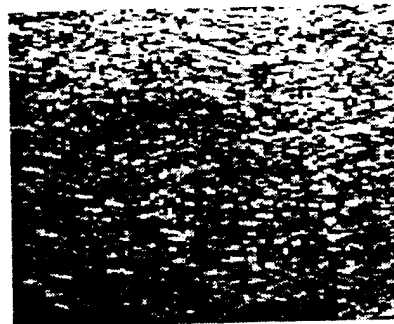


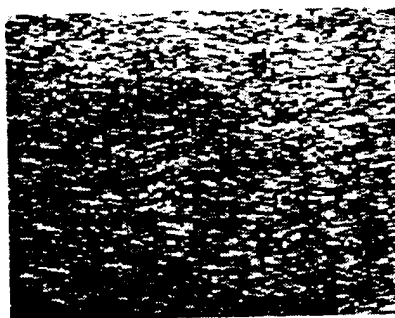
Fig.7 Shaded auto-covariance function of the RF-data corresponding to: (a) the original image shown in Fig. 5(a); (b) the laterally and axially deconvolved image shown in Fig. 5(d). Absolute values of the auto-covariance functions have been shown for easy visualization. (c) The lateral slice L_{00} and (d) the axial slice A_{00} of the auto-covariance function corresponding to: the original image (solid lines), the deconvolved image (dotted lines).



(a)



(b)



(c)

Fig.8 (*Experiment (D)*): (a) A part of the clinical image of a human liver containing a tumor; (b) the result of lateral deconvolution and (c) the result of lateral and axial deconvolution. In all cases the logarithm of the envelope is shown. Deconvolution was performed with the **higher-order** statistics based estimated distortions.

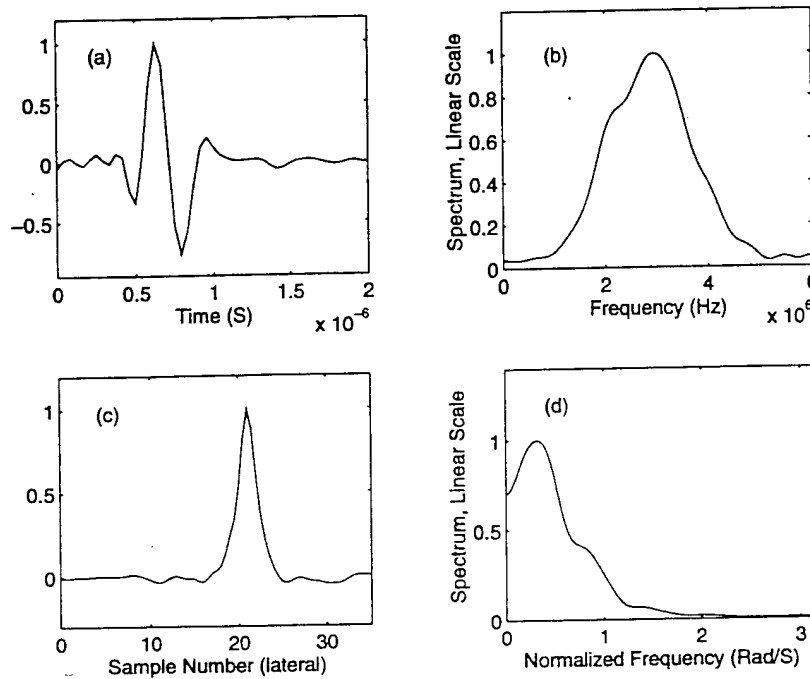


Fig.9 (*Experiment (D)*): (a) The average of the estimated axial kernels from RF-data corresponding to image shown in Fig. 8(a), and (b) its spectrum. (c) The average of the lateral kernels estimated from RF-data corresponding to Fig. 8(a) and (d) its spectrum.

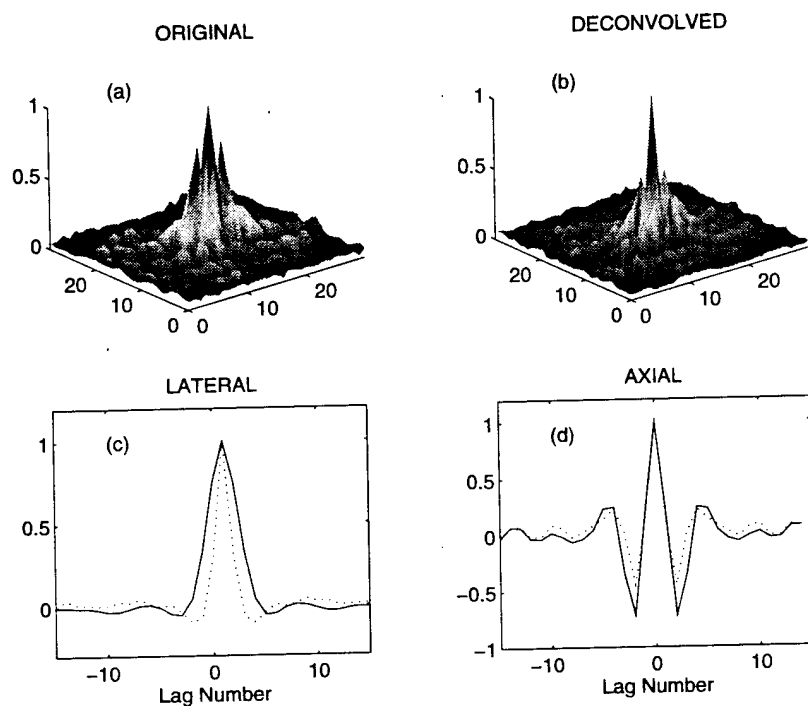


Fig.10 Shaded auto-covariance function of the RF-data corresponding to: (a) the original image shown in Fig. 8(a); (b) the laterally and axially deconvolved image shown in Fig. 8(d). Absolute values of the auto-covariance functions have been shown for easy visualization. (c) The lateral slice L_{00} and (d) the axial slice A_{00} of the auto-covariance function corresponding to: the original image (solid lines), the deconvolved image (dotted lines).

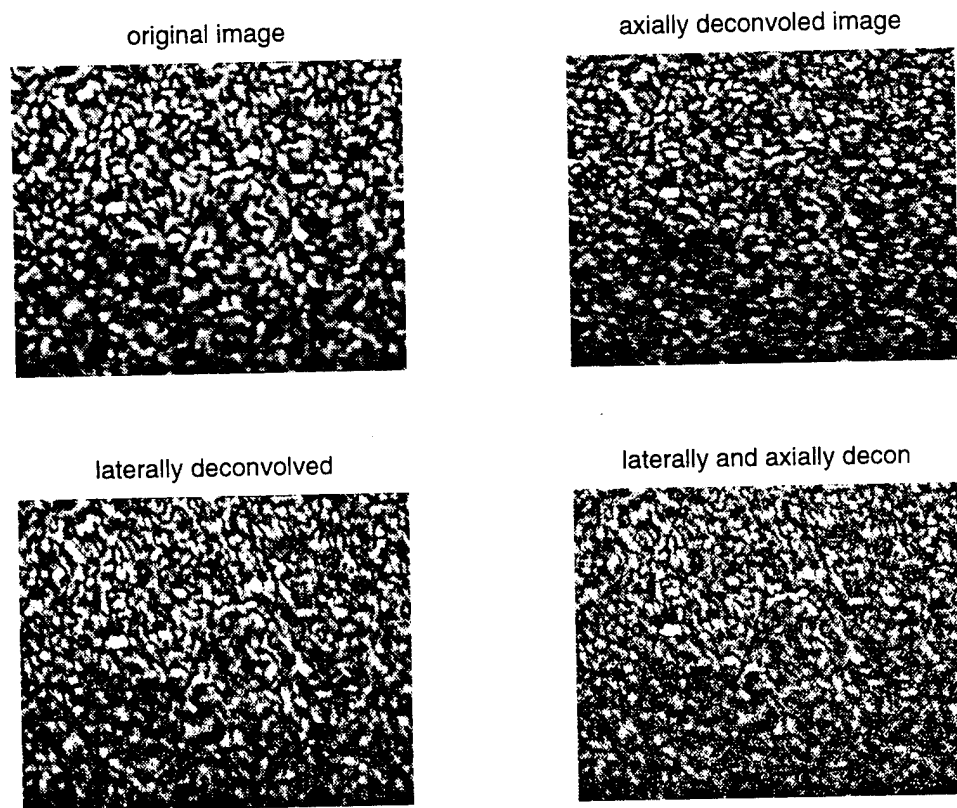


Fig.11 A speckle-only part of the ultrasound image of the tissue mimicking phantom, obtained with a focused single element transducer *experiment* (A); (b) the result of lateral deconvolution; (c) the result of axial deconvolution and, (d) the result of lateral followed by axial deconvolution. In all cases, the logarithmically compressed envelope is shown. Deconvolution was performed with the **second-order statistics** based estimated distortions.

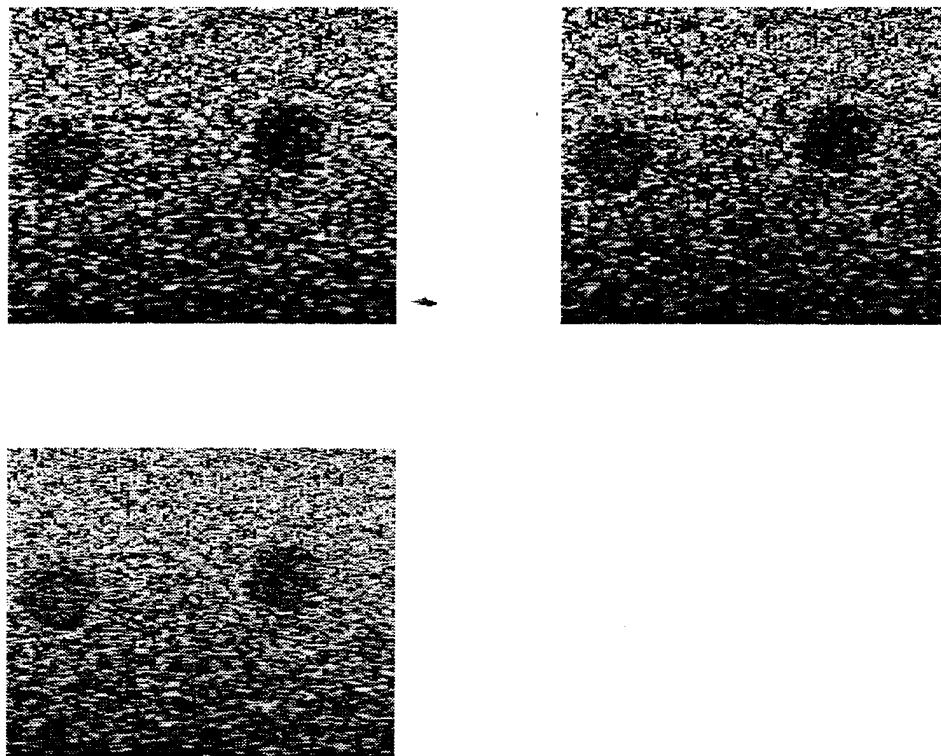


Fig.12 (*Experiment (C)*): (a) The original image of the tissue mimicking phantom obtained with the linear array transducer on a clinical imaging system; (b) the result of lateral deconvolution and (c) the result of lateral and axial deconvolution. The logarithmically compressed envelope has been used for display. Deconvolution was performed with the **second-order statistics** based estimated distortions.

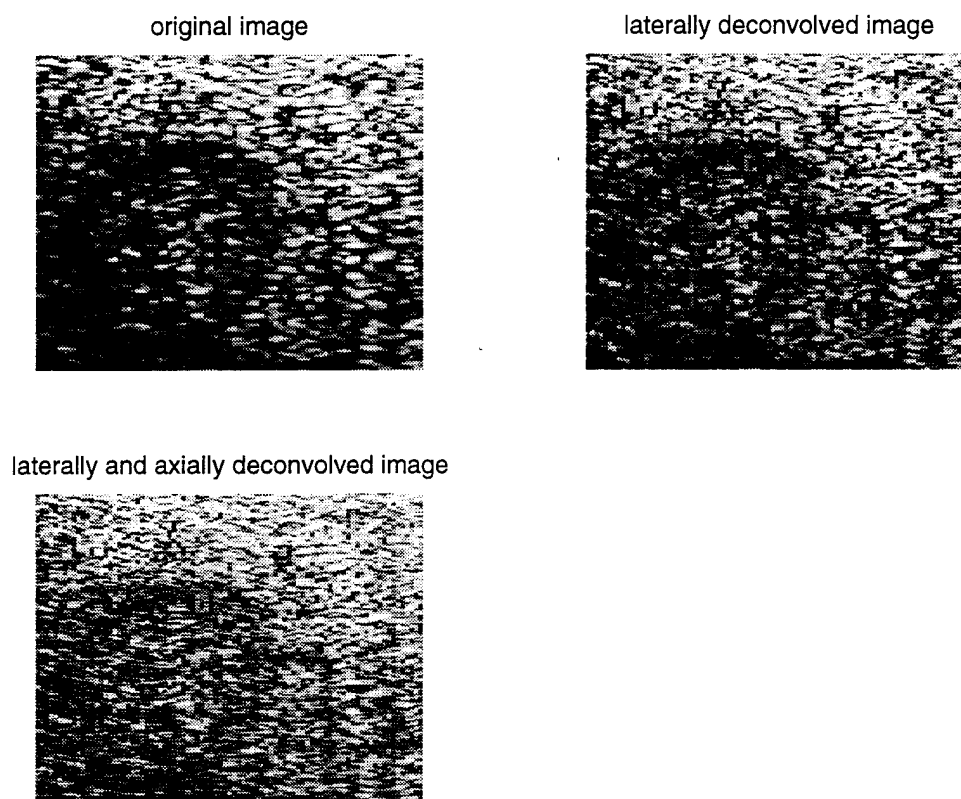


Fig.13 (*Experiment (D)*): (a) A part of the clinical image of a human liver containing a tumor; (b) the result of lateral deconvolution and (c) the result of lateral and axial deconvolution. In all cases the logarithm of the envelope is shown. Deconvolution was performed with the **second-order statistics** based estimated distortions.

Table 1: Resolution gains due to deconvolution with HOS-based estimated distortions

	Resolution Gains			
	<i>lateral</i>		<i>axial</i>	
	5dB	10dB	5dB	10dB
<i>Experiment (A)</i>	2.7	3.0	1.7	1.7
<i>Experiment (C)</i>	5.2	4.2	1.8	1.9
<i>Experiment (D)</i>	3.0	2.5	1.7	1.5

Table 2: The effect of deconvolution with HOS-based distortions on the speckle SNR ratio

	SNR	
	<i>original</i>	<i>deconvolved</i>
<i>Experiment (A)</i>	1.24	1.26
<i>Experiment (C)</i>	1.17	1.10
<i>Experiment (D)</i>	1.20	1.30

Table 3: The effect of deconvolution with SOS-based distortions on the speckle SNR ratio

	Resolution Gains			
	<i>lateral</i>		<i>axial</i>	
	5dB	10dB	5dB	10dB
<i>Experiment (A)</i>	1.6	1.35	1.53	1.20
<i>Experiment (C)</i>	1.85	0.93	1.48	1.64
<i>Experiment (D)</i>	1.50	1.44	1.50	1.23

Table 4: The effect of deconvolution with SOS-based distortions on the speckle SNR ratio

	SNR	
	<i>original</i>	<i>deconvolved</i>
<i>Experiment (A)</i>	1.21	1.24
<i>Experiment (C)</i>	1.2	1.20
<i>Experiment (D)</i>	1.10	1.17

10 PUBLICATIONS

Journal publications supported by this grant during 1994-1995

- A.P. Petropulu, "Higher-Order Spectra in biomedical signal processing," *CRC Press Biomedical Engineering Handbook*, 1995.
- U.R. Abeyratne, A.P. Petropulu and J.M. Reid, "Higher Order Spectra Based Deconvolution of Ultrasound Images", *IEEE Transactions on UFFC*, to appear in 1995.
- U.R. Abeyratne, A.P. Petropulu and J.M. Reid, "On Modeling the Tissue Response From Ultrasonic B-Scan Images," *IEEE Transactions on Medical Imaging*, submitted in February 1995, revision requested on July 1995.
- T. Golas, A.P. Petropulu, J.M. Reid, "In-vivo distortion estimation from ultrasound images: a comparative study of autocorrelation based versus higher-order statistics based methods," to be submitted to the *IEEE Trans. on UFFC*.

Conference proceedings publications supported by this grant during 1994-1995

- U.R. Abeyratne, A.P. Petropulu and J.M. Reid, "Blind Deconvolution of Ultrasound Images," *SPIE International Symposium on Optics, Imaging and Instrumentation*, San Diego, July 1994.
- U.R. Abeyratne, A.P. Petropulu, J.M. Reid and T. Golas, "Estimating Imaging Distortions and Tissue Response From Ultrasonic Images," *20th International Symposium on Ultrasonic Imaging and Tissue Characterization*, Arlington, VA, June 1995.
- U.R. Abeyratne, A.P. Petropulu and J.M. Reid, "Higher Order Spectra Based Deconvolution of Ultrasound Images," *IEEE Workshop on Nonlinear Signal and Image Processing*, Neos Marmaras, Greece, June 1995.
- U.R. Abeyratne, A.P. Petropulu and J.M. Reid, "Higher Order Spectra Based Deconvolution of Ultrasound Images," *IEEE Workshop on Nonlinear Signal and Image Processing*, Neos Marmaras, Greece, June 1995.
- U.R. Abeyratne and A.P. Petropulu, " α -Weighted Cumulant Projections: a Novel Tool for System Identification," *29th Annual Asilomar Conference on Signals, Systems and Computers*, California, October 1995.

- T. Golas, A.P. Petropulu, J.M. Reid, "In-vivo distortion estimation from ultrasound images: a comparative study of autocorrelation based versus higher-order statistics based methods," *Intern. Conf. on Acoustics Speech and Signal Processing*, ICASSP-96, Atlanta GA, 1996, submitted.

MEETING ABSTRACTS

SPIE International Symposium on Optics, Imaging and Instrumentation, San Diego, July 1994.

Blind Deconvolution of Ultrasound Images

Udantha R. Abeyratne, Athina P. Petropulu and John M. Reid*

Biomedical Engineering and Science Institute

*Department of Electrical and Computer Engineering,

Drexel University, Philadelphia, PA 19104

We address the problem of improving the resolution of ultrasound images using blind deconvolution. The transducer measurement that forms the ultrasound image can be expressed as the convolution of two terms, the tissue response and the ultrasonic system response, plus additive noise. The quantity of interest is the tissue response, however, due to the convolution operation, we measure a blurred version of it, which obscures the fine details in the image. Our goal is to remove the blurring caused by the ultrasonic system, in order to enhance the diagnostic quality of the ultrasound image. Under the assumption that speckle behaves as an i.i.d. zero-mean non-Gaussian process, we were able to reconstruct the blurring kernel using bicepstrum operations on corresponding A-scan lines. Based on the estimated blurring kernel we performed deconvolution on the measured image. Preliminary results obtained from ultrasound images of a tissue mimicking phantom indicate significant resolution improvement.

20th International Symposium on Ultrasonic Imaging and Tissue Characterization, Arlington, VA, June 1995.

Estimating Imaging-Distortions and the Color of the Tissue Response From Ultrasonic Images

Udantha R. Abeyratne, Athina P. Petropulu, John M. Reid and Thomas Golas**

Biomedical Engineering and Science Institute

*Department of Electrical and Computer Engineering,

Drexel University, Philadelphia, PA 19104

We address the problem of estimating imaging-distortions and modeling the tissue response from clinical B-scan ultrasound images, based on rf A-lines that form the image. We

model rf A-lines as: $y_i(n) = h_i(n) * f_i(n) + w_i(n)$, $i = 1, 2, \dots$, where $y_i(n)$ is the observed rf A-line, $f_i(n)$ is the tissue response, $w_i(n)$ is the observation noise and $h_i(n)$ is the kernel representing imaging distortions; the symbol '*' stands for the convolution operation. The following assumptions are made: [A1] $h_i(n)$ is deterministic, possibly non-minimum phase, [A2] $f_i(n)$ is stationary, zero-mean non-Gaussian, modeled as the convolution of a white component $e_i(n)$ and a deterministic part $t_i(n)$ corresponding to the statistical color of the tissue response, [A3] $w_i(n)$ is zero-mean, Gaussian, and independent of $f_i(n)$. A colored random process is taken as the model for the tissue response, considering the fact that underlying scatterers need not be randomly and independently located. Applying higher order spectra based blind deconvolution on pairs of closely located rf A-lines, we identify the color of the tissue response as well as the distortion kernels. The color of the tissue response is independent of the imaging system and can be used in tissue characterization. We estimate distortion kernels and the color of the tissue response, from a B-mode image of a human liver, containing a tumor. The statistical color of the tissue response estimated inside the tumor has features that are distinctly different from those estimated outside the tumor. This may be attributed to the change in the tissue structures brought about by the tumor. Our kernel estimation and color identification process is based on data from regions as small as 12 mm^2 (approx.) in the tissue space. The advantages of the proposed approach are: (a) since the estimations are carried out in higher order spectra domain, results are immune to additive Gaussian noise in observations, and (b) both minimum phase and non-minimum phase kernels can be estimated. We compare our method with existing non-parametric pulse estimation techniques and demonstrate relative strengths and weaknesses.

IEEE Workshop on Nonlinear Signal and Image Processing, Neos Marmaras, Greece, June 1995.

Higher Order Spectra Based Deconvolution of Ultrasound Images

Udantha R. Abeyratne, Athina P. Petropulu[†], John M. Reid

Biomedical Engineering and Science Institute

[†] Electrical and Computer Engineering Department

Drexel University, Philadelphia, PA 19104

Our goal is to model and identify the tissue response based on the backscattered rf signal that forms the ultrasound image. We model the rf ultrasonic image, in both axial and lateral directions, as the convolution between an 1-D hypothetical tissue response and

the ultrasonic system response (distortion), plus additive Gaussian noise. We model the tissue response as a non-Gaussian, colored random process. Closely spaced axial (lateral) image lines contain as a common convolutional term the axial (lateral) distortion, whereas the noncommon terms are due to the tissue color. Applying blind deconvolution, we identify the color of the tissue response as well as the corresponding distortion kernels. The color of the tissue response is independent of the imaging system and can be used as a tissue characterization parameter. Estimated kernels are compared with experimentally obtained kernels, and the deconvolution of real ultrasound images is performed.

Asilomar 1995, submitted

α -Weighted Cumulant Projection: A New Tool For System Identification

*Udantha R. Abeyratne and Athina P. Petropulu**

Biomedical Engineering and Science Institute

*Department of Electrical and Computer Engineering,

Drexel University, Philadelphia, PA 19104

Summary

It is well established that identification of a nonminimum phase non-Gaussian random process can be achieved based on its higher-order cumulants (order three or higher). We propose a computationally attractive approach for system identification, whose complexity remains constant as the order of the employed cumulants increases. We define the **α -weighted n^{th} -order cumulant projection** of the process $x(k)$ to be

$$p_n^x(\tau; \alpha) = \sum_{\tau_2} \dots \sum_{\tau_{n-1}} c_n^x(\tau, \tau_2, \dots, \tau_{n-1}) \alpha^{\tau + \tau_2 + \dots + \tau_{n-1}}, \quad \alpha : \text{complex}, |\alpha| = 1, \quad (15)$$

where $c_n^x(\cdot)$ denotes n^{th} order cumulant. For the process

$$x(k) = h(k) * e(k), \quad (16)$$

where $e(k)$ is white non-Gaussian zero-mean, and $h(k)$ is deterministic generally nonminimum phase, we prove that

$$P_n^x(z; \alpha) = c H(\alpha^{-1} z) H(\alpha^{(n-1)} z^{-1}), \quad (17)$$

where $P_n^x(z; \alpha)$ is the Z-transform of $p_n^x(\tau; \alpha)$, and c is a constant. From (17), it can be shown that by controlling α , $H(z)$ can be identified for $n > 2$. If $\hat{p}_n^x(k; \alpha)$ and $\hat{h}(k)$ denote

the complex cepstra of $p_n^x(\tau; \alpha)$ and $h(k)$, respectively, we show that

$$\hat{h}(k) = \frac{\hat{p}_n^x(k; \alpha) - \alpha^{(n-1)k} \hat{p}_n^x(k; 1)}{\alpha^k - \alpha^{(n-1)k}}, \quad k > 0 \quad (18)$$

$$\hat{h}(-k) = \frac{-\hat{p}_n^x(k; \alpha) + \alpha^k \hat{p}_n^x(k; 1)}{\alpha^k - \alpha^{(n-1)k}}, \quad k > 0, \quad (19)$$

which leads to a scaled and shifted version of $h(k)$ via inverse cepstrum operations. We show that we can always find a complex number α with unit magnitude to guarantee that the denominator in (18) and (19) is different from zero, and discuss the rationale behind choosing a particular value for α .

Based on equation (17) a formula for the estimation of the Fourier phase of $h(k)$ from the phase of the α -weighted cumulant projection is also derived.

11 PERSONNEL

John M. Reid, Drexel University

Athina P. Petropulu, Drexel University

Udantha Abeyratne, Drexel University

Thomas Golas, Drexel University

Vladimir Genis

Christopher Wendt, Drexel University